Available online at www.sciencedirect.com
ScienceDirect
International Journal of Thermal Sciences 47 (2008) 787–799
International Journal of Thermal Sciences
www.elsevier.com/locate/ijts

Effective cooling of stacked heat-generating bodies in a large room: Comparison between floor and side-wall air injection

J.R. Berg, H.M. Soliman *, S.J. Ormiston

Department of Mechanical and Manufacturing Engineering, University of Manitoba, Winnipeg, Manitoba, Canada R3T 5V6

Received 6 February 2007; received in revised form 19 April 2007; accepted 8 June 2007

Available online 13 July 2007

Abstract

A numerical investigation of the air flow and heat transfer phenomena in a ventilated converter valve hall has been carried out using the k–ε turbulence model with scalable wall functions. The geometry involving a large building enclosing heat-generating blocks in three towers (16 tiers each) with inlet and outlet openings was simulated as a three-dimensional domain. Results were obtained for the base case simulating the currently existing conditions in the valve hall and six other cases corresponding to various geometry and inlet flow parameters in an attempt to enhance the current cooling effectiveness. These results include the net air flow in all 15 tower gaps and the maximum temperature in each gap. It is demonstrated that significant improvements in the cooling effectiveness with large reduction in the temperature of the tower surfaces can be achieved without having to increase the inlet air flow rate into the valve hall.

Keywords: Numerical simulation; Turbulent mixed convection; Three-dimensional geometry; DC/AC converter valve hall; Ventilation; Cooling effectiveness

1. Introduction

High-Voltage-Direct-Current (HVDC) transmission systems have become more desirable in today's electricity industry because of environmental and economical advantages, improved power flow control, and other added benefits related to stability and power quality. Currently, large amounts of power are transmitted via HVDC systems in several countries around the world (e.g., Argentina, Australia, Brazil, Canada, India, Philippines, and Sweden). The fundamental process that occurs in an HVDC system is the conversion of electrical current from AC to DC at the transmitting end, and from DC to AC at the receiving end. In most systems, the AC/DC and DC/AC conversions are achieved in converter stations using an electronic device called the "thyristor" valve. A typical converter station consists of a number of converter valve halls; each valve hall is a large building housing stacks of thyristor valves. Due to electrical losses in the conversion process, large amounts of heat are generated in the thyristor valves and therefore, an effective cooling system must be installed in order to keep the electronics (thyristors) at or below their design operating temperature.

This investigation relates to a DC/AC converter station near Winnipeg, Canada that handles 3854 MW of power. This conversion process is performed in a number of valve halls, one of which, with a capacity of 500 MW, is the subject of this study. The heat generated during the conversion process is removed by a combination of water cooling applied internally to the thyristor valves and air cooling applied by injecting cold air through grills in the floor of the building and rejecting the return warm air from the ceiling. Occasionally, particularly during summer operation, a high temperature level has been reported in the valve hall, especially near the thyristor valve modules. A simple energy balance on the air indicated that the input air flow rate used in the valve hall is adequate because the bulk-temperature difference between inlet and outlet was about 23 °C. However, the pattern of air flow within the valve hall, particularly in the vicinity of the thyristor valve, is not known and, to the authors' best knowledge, has not been investigated before.

Developing solutions for the air flow and temperature distributions in converter valve halls requires a numerical study of mixed-convection cooling during turbulent air flow over three-dimensional heated structures. This type of research is not only

* Corresponding author. Tel.: +1 204 474 9307; fax: +1 204 275 7507.
E-mail address: hsolima@cc.umanitoba.ca (H.M. Soliman).

1290-0729/$ – see front matter
doi:10.1016/j.ijthermalsci.2007.06.007

Nomenclature

A	area	m^2
C_p	specific heat	$J\,kg^{-1}\,K^{-1}$
$C_{\varepsilon 1}$	k–ε turbulence model constant	
$C_{\varepsilon 2}$	k–ε turbulence model constant	
C_μ	k–ε turbulence model constant	
g	gravitational acceleration	$m\,s^{-2}$
I	turbulence intensity	
k	turbulence kinetic energy per unit mass	$m^2\,s^{-2}$
L_1	length of floor opening in the x direction	m
L_2	length of floor opening in the y direction	m
L_3	location of floor opening relative to domain CD1 boundary	m
L_4	length of side-wall opening in the x direction	m
L_5	length of side-wall opening in the z direction	m
L_6	location of side-wall opening relative to domain CD2 boundary	m
$\dot{m}$	mass flow rate	$kg\,s^{-1}$
P	time-averaged pressure	Pa
P_k	turbulence production	$kg\,m^{-1}\,s^{-3}$
P^*	time-averaged dynamic pressure	Pa
q''	uniform heat flux at the block surfaces	$W\,m^{-2}$
R	viscosity ratio	
T	temperature	K
T_{max}	maximum temperature in the domain	K
u	time-averaged velocity component in the x direction	$m\,s^{-1}$
v	time-averaged velocity component in the y direction	$m\,s^{-1}$
V_{jet}	resultant jet velocity at the inlet opening	$m\,s^{-1}$
w	time-averaged velocity component in the z direction	$m\,s^{-1}$
x, y, z	Cartesian coordinate system	m

Greek letters

ε	turbulence dissipation rate	$m^2\,s^{-3}$
ρ	density	$kg\,m^{-3}$
μ	viscosity	$kg\,m^{-1}\,s^{-1}$
μ_t	eddy viscosity	$kg\,m^{-1}\,s^{-1}$
λ	thermal conductivity	$W\,m^{-1}\,K^{-1}$
θ	angle of inlet air jet with the horizontal	
σ_ε	k–ε turbulence model constant	
σ_k	k–ε turbulence model constant	

Subscripts

CA	Case A
g	gap
o	inlet

relevant to DC/AC converter halls, but also relevant to the packaging of electronic devices, the design of power transformers, and the design of cooling systems for spent nuclear fuel. Unfortunately, due to the complexity of the flow in these applications, relatively few studies have been done on this topic. Most of the studies that have been attempted on this topic involve a simplified geometry (e.g., a two-dimensional flow domain) and/or a simplified flow structure (e.g., laminar flow or pure free convection), which limits their value in real world applications.

Li and Chung [1] studied laminar two-dimensional mixed convection of air in a vertical rectangular channel with heated blocks to simulate the cooling of electronics packages. The authors investigated the effect of varying Rayleigh number with a fixed inlet mass flow rate on the overall cooling effectiveness. Shuja et al. [2] investigated two-dimensional mixed convection of air in a square cavity with a single heat generating body. In that study, the effects of cavity exit-port locations on heat transfer and entropy generation for two body aspect ratios were considered. Bhoite et al. [3] studied two-dimensional laminar mixed convection of air in an enclosure with a series of heat generating blocks. The authors found that for a given heat generation rate, the maximum surface temperatures typically decreased with increasing mass flow rate. For very high heat generation rates, however, maximum surface temperatures initially increased followed by a decrease at higher mass flow rates. Bellache et al. [4] numerically studied two-dimensional turbulent ventilation patterns and thermal processes in an ice rink. The standard k–ε model was used to model the turbulence quantities. It was determined that the location of the inlet and outlet ducts as well as the orientation of the inlet air can have a large effect on the heating load, the humidity, and the comfort of the spectators in the ice rink. Later, Bellache et al. [5] considered two different positions of the air outlet and found that the position initially envisaged in the architectural plans resulted in higher heat losses and a higher refrigeration load for the ice rink. However, neither of the two air outlet positions gave satisfactory results as far as air renewal in the area occupied by the spectators. Ramirez-Iraheta et al. [6] investigated the two-dimensional laminar flow of air inside a cavity with a single inlet and a single outlet enclosing towers made up of heat-generating rectangular blocks. The effects of the number, position, and size of the towers, the inlet mass flow rate, and the location of the inlet and outlet openings on the velocity and temperature distributions within the domain were considered. The results showed that the position of the towers with respect to the inlet and outlet openings had a significant impact on the velocity and temperature in the domain with the tower locations that provided the lowest block temperatures being the ones that maximized the air flow between the blocks. Ramirez-Iraheta et al. also found that the inlet mass flow rate had a significant effect on the velocity and temperature in the domain.

The present investigation deals with the effective three-dimensional turbulent air-side cooling of vertical stacks, or towers, of heat generating bodies. As the valve hall to be modeled is already in existence, the size of the room as well as the size, location, and orientation of the towers are assumed to be fixed

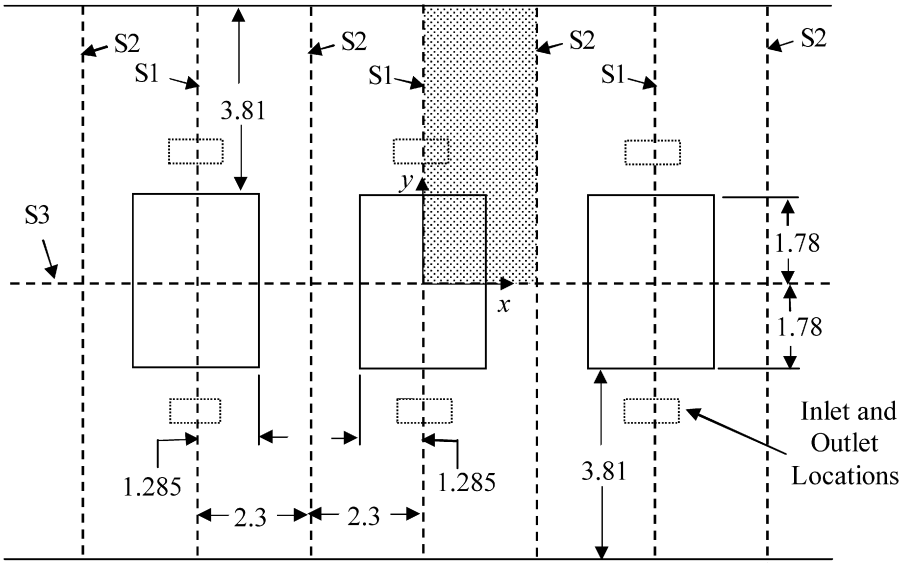

Fig. 1. Plan view of the simulated DC/AC valve hall (dimensions in meters).

quantities. The inlet and outlet air openings are located on the floor and ceiling of the domain, respectively, in the existing valve hall. The air conditioning units for the room are also already in existence, therefore an ideal solution would be one in which the current inlet air flow rate was maintained. As a first attempt towards improving the cooling effectiveness over the current conditions in the existing valve hall, the present authors limited their work to floor injection and explored the effects of simple modifications of the angle of injection of the inlet air jet, the area of the inlet air grills, and the inlet mass flow rate [7]. Thus, the work in [7] corresponds to minimal structural changes in the existing valve hall. In the present study, other methods for enhancing the cooling effectiveness involving substantial structural changes (e.g., side-wall injection) are considered. The main objective of the present work is to compare the cooling effectiveness achievable by side-wall injection with that of floor injection. In addition to the method of air injection, other parameters that were varied during the course of the present work are the size and location of the inlet and outlet openings as well as the angle of injection of the inlet air.

2. Mathematical formulation

Fig. 1 shows a plan view of the flow domain under consideration in this study with dimensions that are similar to an existing valve hall in a converter station. The domain is bounded by two walls that are separated by a distance of 11.18 m in the y direction and a ceiling that is 13.35-m high (in the z direction). The walls on the right- and left-sides of the domain were replaced by symmetry planes in order to introduce symmetry and significantly reduce the computation time. Towers consisting of 16 heat-generating blocks are housed inside the domain. These towers are 2.57 m × 3.56 m × 7.98 m in the x, y, and z directions, respectively. Each block is 0.33-m thick and successive blocks are separated by a distance of 0.18 m. In Fig. 1, the cooling air is brought into the domain through grills in the floor and

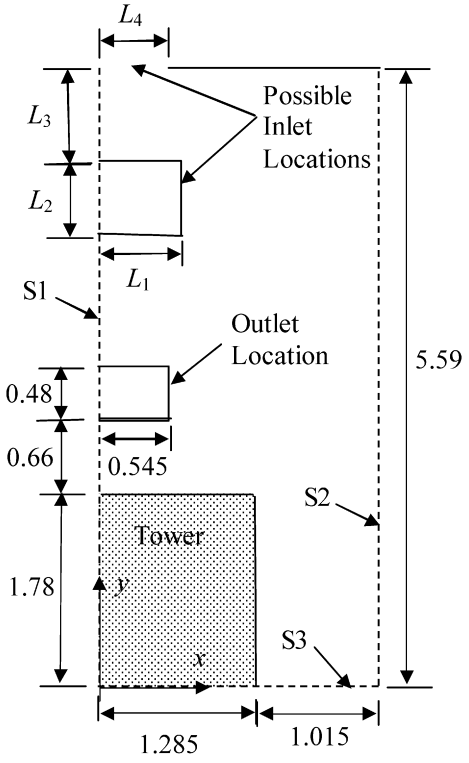

Fig. 2. Plan view of CD1 (dimensions in meters).

the return warm air is rejected through outlets in the ceiling, which is the case in the present valve-hall design.

Two methods of air injection, floor and side-wall injection, will be considered in this study. When the inlet- and outlet-air openings are symmetrical with the tower center line on the x and y axes, planes S1, S2, and S3 in Fig. 1 become symmetry planes, and Computational Domain 1 (CD1) was used in the computations. A description of CD1 is shown in Figs. 2 (plan view) and 3 (elevation view). On the other hand, when the inlet and outlet openings are symmetrical with the tower

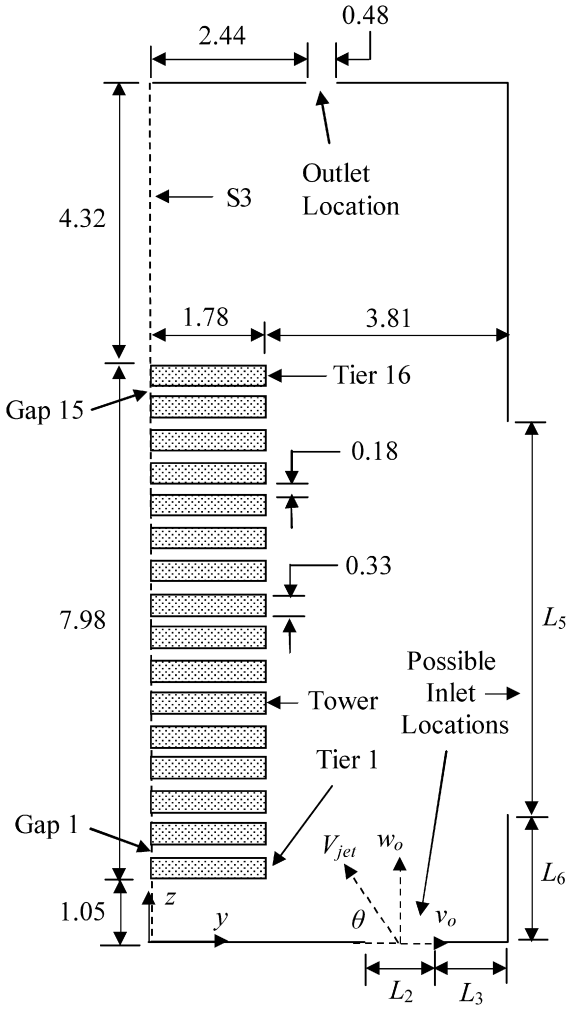

Fig. 3. Elevation view of CD1 (dimensions in meters).

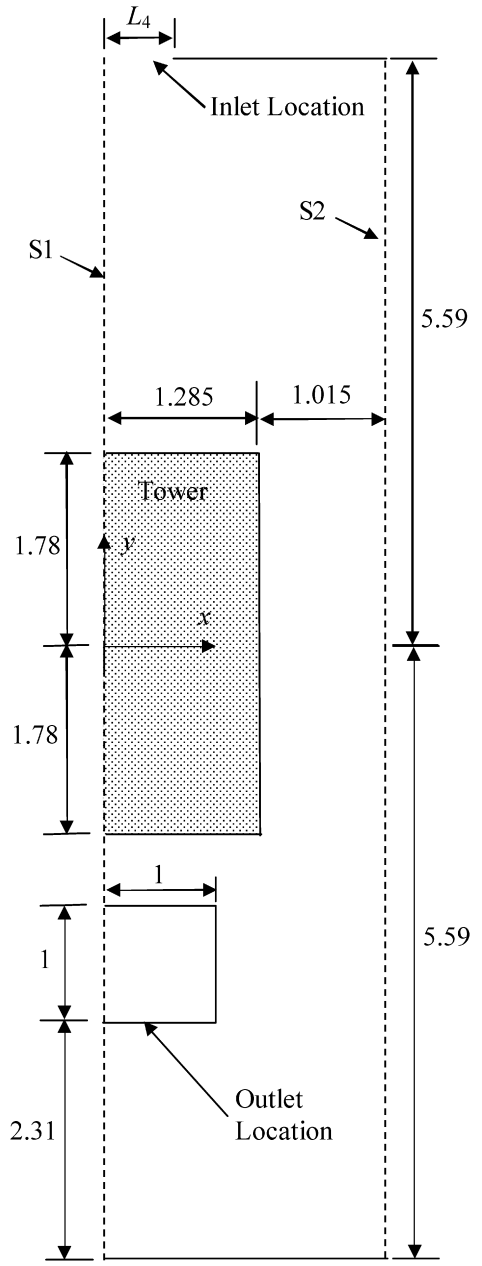

Fig. 4. Plan view of CD2 (dimensions in meters).

centerline on only one axis (the y axis), symmetry exists on planes S1 and S2 in Fig. 1, but not on plane S3. For such cases, Computational Domain 2 (CD2) was used and its description is shown in Figs. 4 (plan view) and 5 (elevation view). The overall dimensions of the cavity and the tower are fixed for both computational domains.

One inlet opening is modeled for CD1. This inlet opening can either be on the floor or the side wall of the domain, but not on both. The centre line of this opening is on symmetry plane S1. When the inlet opening is located on the bottom of the domain, its location is defined by length L_3 and its size is defined by lengths L_1 and L_2 in the x and y directions, respectively. When the inlet opening is located on the side wall of the domain, its location is defined by length L_6 and its size is defined by lengths L_4 and L_5 in the x and z directions, respectively. One outlet opening is also modeled for CD1. The location and size of this opening is fixed with the dimensions indicated in Figs. 2 and 3.

For CD2, one side-wall inlet opening is also modeled with its centre line located on symmetry plane S1. Its location is defined by length L_6 and its size is defined by lengths L_4 and L_5 in the x and z directions, respectively. One outlet opening is also modeled for CD2 with fixed size and location, as shown in Figs. 4 and 5.

For both computational domains, the thyristor tower is modeled as a series of sixteen stacked vertical blocks. The distance from the floor to the bottom of the first block is 1.05 m in the z direction. A uniform heat flux q'' is applied at the surfaces of the blocks, while all cavity walls are insulated.

2.1. Governing equations

The flow is considered to be three-dimensional, steady, and turbulent. The fluid is assumed to be Newtonian with constant fluid properties, except for the density ρ in the expression of the body forces. The eddy-viscosity approximation was used to model the Reynolds stresses in the momentum equations. Under

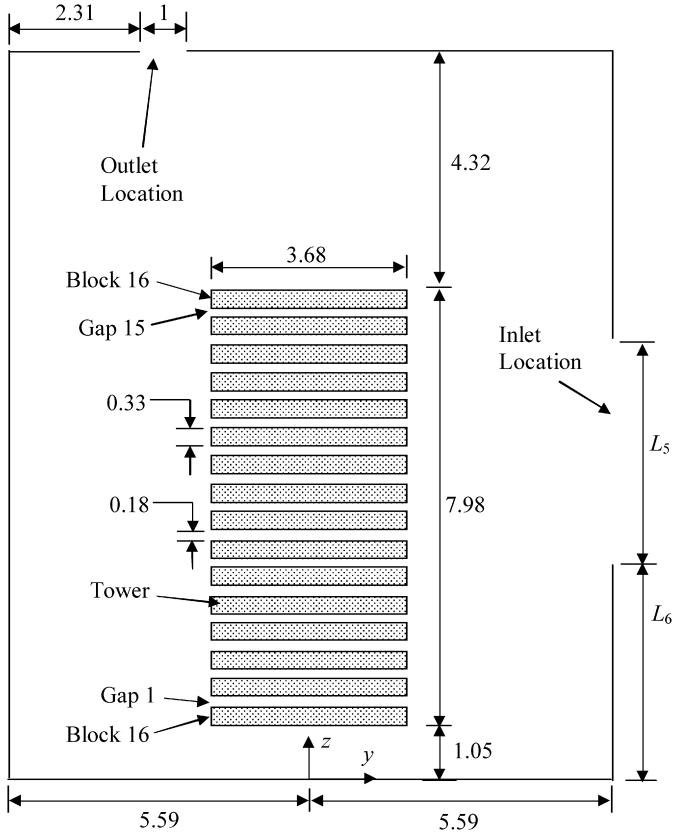

Fig. 5. Elevation view of CD2 (dimensions in meters).

these conditions, the time-averaged equations for the conservation of mass, momentum and energy are applicable. These governing equations, also known as the Reynolds-averaged Navier–Stokes equations, can be expressed in tensor form as:

$$\text{Momentum:}\quad \rho\left(u_j\frac{\partial u_i}{\partial x_j}\right) = -\frac{\partial P}{\partial x_i} + \frac{\partial}{\partial x_j}\left((\mu+\mu_t)\frac{\partial u_i}{\partial x_j}\right) + \rho g_i, \quad i = 1,2,3 \tag{1}$$

$$\text{Continuity:}\quad \frac{\partial u_j}{\partial x_j} = 0 \tag{2}$$

$$\text{Energy:}\quad u_j\frac{\partial T}{\partial x_j} = \frac{\partial}{\partial x_j}\left(\frac{\lambda}{\rho C_p}\frac{\partial T}{\partial x_j}\right) \tag{3}$$

where u_i are the Cartesian time-averaged velocity components with the commonly used over-bars omitted for convenience ($u_1 = u$, $u_2 = v$, and $u_3 = w$), P is the time-averaged pressure with the over-bar also omitted for convenience, $g_i = -9.8\ \text{m/s}^2$ for $i = 3$, and $g_i = 0$ for $i = 1$ and 2.

Splitting the pressure into dynamic (P^*) and hydrostatic components:

$$P^* = P - \rho_o g_i z \tag{4}$$

the resulting momentum equations can be written as:

$$\rho\left(u_j\frac{\partial u_i}{\partial x_j}\right) = -\frac{\partial P^*}{\partial x_i} + \frac{\partial}{\partial x_j}\left((\mu+\mu_t)\frac{\partial u_i}{\partial x_j}\right) + (\rho-\rho_o)g_i, \quad i = 1,2,3 \tag{5}$$

where ρ_o is the density of the air at the inlet.

2.2. Turbulence closure

An extension of the standard k–ε model of Launder and Spalding [8] with the scalable-wall-function approach of Grotjans and Menter [9] were chosen for the computations. This choice was based on the results of Berg et al. [10], who compared the predictions based on the k–ε and the k–ω turbulence models against the experimental results of Quinn [11] for an isothermal rectangular free jet. Berg et al. found that the k–ε model produced more accurate results. As well, a comparison is presented later on between the predictions of the present model and experimental results as further validation of the present approach.

In the k–ε model, the eddy viscosity is computed using the relation:

$$\mu_t = C_\mu \rho \frac{k^2}{\varepsilon} \tag{6}$$

where C_μ is a constant and the values of k and the dissipation, ε, come from the solution of the following transport equations:

$$\rho u_i\frac{\partial k}{\partial x_i} = \frac{\partial}{\partial x_i}\left(\mu+\frac{\mu_t}{\sigma_k}\right)\frac{\partial k}{\partial x_i} + P_k - \rho\varepsilon \tag{7}$$

$$\rho u_i\frac{\partial \varepsilon}{\partial x_i} = \frac{\partial}{\partial x_i}\left(\mu+\frac{\mu_t}{\sigma_\varepsilon}\right)\frac{\partial \varepsilon}{\partial x_i} + P_k + \frac{\varepsilon}{k}(C_{\varepsilon 1}P_k - C_{\varepsilon 2}\rho\varepsilon) \tag{8}$$

and the turbulence production term, P_k, is modeled using:

$$P_k = \mu_t\frac{\partial u_i}{\partial x_j}\left(\frac{\partial u_i}{\partial x_j} + \frac{\partial u_j}{\partial x_i}\right) \tag{9}$$

The values for the k–ε equation constants used in this work are: $C_\mu = 0.09$, $C_{\varepsilon 1} = 1.45$, $C_{\varepsilon 2} = 1.9$, $\sigma_k = 1.0$, and $\sigma_\varepsilon = 1.3$. During the course of this investigation, the influence of adding the extra buoyancy-related terms in the turbulence model was tested and found to be insignificant. Therefore, these terms were ignored in the turbulence model.

The scalable wall function approach of Grotjans and Menter [9] was used for modeling the flow near the wall. This approach is an extension of the standard wall function approach of Launder and Spalding [8]. In the log-law region, the near wall tangential velocity U_t is related to the wall shear stress τ_w by means of a logarithmic relation. In the wall function approach, empirical formulas are applied which connect the wall condition with the dependent variables at the first near-wall mesh node which is assumed to lie in the logarithmic region of the boundary layer. The relation for the near wall velocity in the logarithmic region is given by:

$$U_t = (u_\tau/\kappa)\log(y^+) + C \tag{10}$$

where the non-dimensional wall distance, y^+, is defined as $y^+ = \rho u_\tau n/\mu$, the friction velocity, u_τ, is given by $u_\tau = (\tau_w/\rho)^{1/2}$, n is the normal distance to the wall, ($\kappa = 0.41$) is the von Karman constant, and C is a constant that depends on the wall roughness ($C = 5.2$ for a smooth wall).

Using the wall function approach, the near wall turbulence quantities k, ε, and μ_t in the logarithmic region were calculated from:

$$k = u_\tau^2/\sqrt{C_\mu} \tag{11}$$

$$\varepsilon = u_\tau^3/(\kappa n) \tag{12}$$

and

$$\mu_t = \rho\kappa u_\tau n \tag{13}$$

The fundamental principle of the scalable wall function approach of Grotjans and Menter [9] is to limit the value of y^+ near the wall, $\tilde{y}^+$, used in the logarithmic formulation to a value of 11.06. The value of $\tilde{y}^+$ was determined from the intersection of the logarithmic and linear profiles near the wall using: $\tilde{y}^+ = \max(y^+, 11.06)$. The computed $\tilde{y}^+$ value was not allowed to fall below this limit and therefore all mesh points were outside of the viscous sub-layer. As a result, mesh inconsistencies associated with applying the k and ε equations in this region were avoided.

The flux boundary conditions applied at the wall for the scalable wall function approach are as follows:

$$\mu_t \frac{\partial U_t}{\partial n} = -\rho u_\tau \max\left(|u_\tau|, u^*\right) \tag{14}$$

$$\frac{\partial k}{\partial n} = 0 \tag{15}$$

and

$$\frac{\mu_t}{\sigma_\varepsilon}\frac{\partial \varepsilon}{\partial n} = -\frac{1}{\sigma_\varepsilon}\frac{(u^*)^5\rho^2}{\tilde{y}^+\mu} \times \left[\frac{2+e}{2+2e} + F_{\text{cal}}\frac{e}{2}\frac{\sigma_\varepsilon\sqrt{C_\mu}}{\kappa^2}(C_{\varepsilon 2} - C_{\varepsilon 1})\right] \tag{16}$$

with:

$$e = \Delta y^+/\tilde{y}^+ \tag{17}$$

and

$$u^* = C_\mu^{1/4} k^{1/2} \tag{18}$$

In Eqs. (14) to (18), Δy^+ is the actual y^+ value from the wall to the first interior node, F_{cal} is a calibration function based on the coarseness of the mesh, and u^* is an alternative velocity scale used to prevent the flux from going to zero at separation points (which was a problem with the standard wall functions). Another advantage of the scalable wall functions as opposed to the standard wall functions is that scalable wall functions can be applied to arbitrarily fine meshes and allow for consistent mesh refinement independent of Reynolds number. These features were major shortcomings of the standard wall function approach.

2.3. Boundary conditions

The boundary conditions for computational domains CD1 and CD2 are as follows:

- All outer walls are impermeable:

  $u = v = w = 0$ on all outer walls and the bottom wall (excluding the inlet) (19)

- All outer walls are adiabatic:

  $\partial T/\partial z = 0$ on the bottom and top walls (20)

  $\partial T/\partial y = 0$ on the side walls (21)

- All block faces are impermeable and zero slip walls:

  $u = v = w = 0$ on all block faces (22)

- Uniform output heat flux was applied on all block faces:

  $\partial T/\partial x = -q''/\lambda$ on the block faces located at $x = 1.285$ m (23)

  $\partial T/\partial y = -q''/\lambda$ on the block faces located at $y = 1.78$ m (24)

  $\partial T/\partial y = q''/\lambda$ on the block faces located at $y = -1.78$ m (for CD2 only) (25)

  $\partial T/\partial z = -q''/\lambda$ on the top faces of all blocks (26)

  $\partial T/\partial z = q''/\lambda$ on the bottom faces of all blocks (27)

- Symmetry conditions across the symmetry planes:

  $u = \partial v/\partial x = \partial w/\partial x = \partial T/\partial x = 0$ on symmetry planes S1 and S2 (28)

  $v = \partial u/\partial y = \partial w/\partial y = \partial T/\partial y = 0$ on symmetry plane S3 (for CD1 only) (29)

- A specified average pressure was applied at the outlet area:

  $\bar{P}^* = 0$ over the outlet opening (30)

Cooling air entered the cavity through the inlet opening at a uniform temperature of T_o. When the inlet opening was located on the floor of the domain, the inlet velocity had components 0, v_o, and w_o in the x, y, and z directions, respectively, with a resultant jet velocity $V_{\text{jet}} = \sqrt{v_o^2 + w_o^2}$ and an inlet air angle $\theta = \tan^{-1}(-w_o/v_o)$. Uniform distributions of v_o and w_o were imposed at the inlet opening. Thus, $\dot{m}_o = \rho_o(L_1L_2)w_o$, where $\dot{m}_o$ is the inlet mass flow rate. When the inlet opening was located on the side wall of the domain, the inlet air velocity was always directed normal to the inlet opening. In that case, the components of the inlet velocity in the x and z directions, u_o and w_o, respectively, were set to zero, and the component of the inlet velocity in the y direction, v_o, was equal to $-\dot{m}_o/(\rho_o L_4 L_5)$. The inlet turbulent kinetic energy k_o was calculated using:

$$k_o = \frac{3}{2} I_o^2 V_{\text{jet}}^2 \tag{31}$$

where I_o is the inlet turbulence intensity. The inlet dissipation ε_o was calculated using:

$$\varepsilon_o = C_\mu \rho_o \frac{k_o^2}{R_o \mu} \tag{32}$$

where R_o is the inlet viscosity ratio (μ_t/μ).

2.4. Numerical solution

The numerical solution of the governing equations was obtained using the finite volume method of Patankar [12]. Cartesian velocity components were used on a non-staggered grid. Mass conservation discretization was applied on the grid with pressure–velocity coupling based on the work of Rhie and Chow [13], Prakash and Patankar [14], and Schneider and Raw [15]. The high-resolution advection scheme based on the work of Barth and Jesperson [16] was used.

The coupled discretized mass and momentum equations plus the energy and the turbulence model equations were solved iteratively using additive correction multi-grid acceleration. These computations were performed using a commercial CFD code (CFX-5, version 5.7). Solutions were considered converged when the normalized maximum residual of all the discretized equations was less than 1×10^{-5}.

Orthogonal (Cartesian) grids were generated for the solution domains shown in Figs. 2 to 5. Non-uniform grid spacing was employed for the meshes in this study in order to place more nodes in regions where the spatial derivatives of the governing equations are high and fewer nodes where there is very little change in the solution fields from node to node. Mesh refinement was required in this project in the gaps between the blocks with an increased amount of nodes needed in order to obtain a converged solution. The distance between the wall and the first node was also decreased near some of the walls in order to achieve a y^+-value of less than 100 on all walls.

Two methods were used to judge mesh independence of the results; the relative maximum temperature of the domain, $\Delta T_{\max}(= T_{\max} - T_o)$, and the relative temperature, $\Delta T(= T - T_o)$, along six different lines in the domain for CD1 and seven lines for CD2. These lines were located along the x, y, or z directions in regions of substantial temperature variation [17]. For CD1, mesh independence tests were performed using coarse, medium, and fine meshes of 868 005, 1 141 442, and 1 475 794 nodes, respectively. The percentage difference in the value of $\Delta T_{\max}$ between the coarse and medium grids and between the medium and fine grids were 1.74% and 1.01%, respectively. The root-mean-square of the difference in the value of ΔT between the coarse and medium grids along the six lines ranged from 1.83% to 10.3%, while the root-mean-square of the difference in the value of ΔT between the medium and fine grids along the six lines ranged from 0.40% to 1.22%. Based on these results, the medium grid was selected for all computations using CD1. For CD2, mesh independence tests were performed using coarse, medium, and fine meshes of 1 723 484, 2 148 130, and 2 512 420 nodes, respectively. The percentage difference in the value of $\Delta T_{\max}$ between the coarse and medium grids and between the medium and fine grids were 7.48% and 2.24%, respectively. The root-mean-square of the difference in the value of ΔT between the coarse and medium grids along the seven lines ranged from 0.65% to 4.05%, while the root-mean-square of the difference in the value of ΔT between the medium and fine grids along the seven lines ranged from 0.23% to 3.29%. Based on these results, the medium grid was selected for all computations using CD2.

2.5. Experimental validation

2.5.1. Constraints and design requirements

Because of the high voltages associated with thyristor valve halls, safety was an important issue for Manitoba Hydro (the utility that owns and operates the facility) in conducting the experiment in the valve hall and therefore, a number of safety-related restrictions were placed on the testing. Personnel were required to be at least 2.5 m away from the towers and not to be located above a height of 5 m from the floor while the hall was in operation. No equipment (e.g., temperature or velocity measuring devices) could be installed in the valve hall unless it was at a distance of 2.5 m away from the towers and a height of at least 12.3 m above the floor. This ruled out the possibility of installing measuring devices in the space between the towers or in the gaps between the tiers in the towers. Further, the measuring devices could not be electrically conductive or produce an electrical current. With these restrictions in place, the design of a suitable experiment to validate the numerical results proved to be quite challenging.

It was decided that the temperature is the only parameter that could be feasibly measured under the above constraints and that infrared thermography (IT) is the best option for obtaining these measurements in the region above 5 m from the floor. A digital thermometer was used to scan the temperature in the region below 5 m from the floor. In order to use IT for measuring the air temperature at a particular location, an object must be placed in the airfield that would take on the temperature of the air at that location without significantly altering the flow, and then taking a thermal image of that object.

In addition to the restrictions stated above on the possible locations of objects or targets to be placed in the air field, several other requirements were placed on the design of these objects, such as:

(1) the targets must be constructed using an electrically non-conductive material,
(2) a material with a low thermal mass must be used in order to decrease the time required for the object to reach thermal equilibrium with the surrounding air,
(3) the targets must be as non-restrictive to airflow as possible in order to maintain an accurate representation of the air field,
(4) it is desirable to have as many readings of temperature across the airfield as possible (a continuous temperature profile would be ideal, but this may not be possible due to requirement 3), and
(5) in order to limit reflections from neighbouring objects, IT is most accurate when using a highly emissive material as a target.

2.5.2. Locations of temperature measurement

Taking the above restrictions and requirements into account, a number of areas were selected for IT testing. Area 1 was located on thin plastic covers, a small distance away from the surface of the towers. Referring to Fig. 1, this area corresponds to $x = 0.64$ m, $y = 1.81$ m to 1.84 m, and various values of z.

Square patches (10 cm × 10 cm) of black Scotch™ Super 88 electrical tape ($\varepsilon_s = 0.98$), were attached to the plastic covers at these locations in Area 1. Area 2 was a horizontal plane located above the thyristor towers at $-2.71\ \text{m} \leqslant x \leqslant 2.71\ \text{m}$, $0 \leqslant y \leqslant 5.59$ m, and $z = 12.28$ m (see Fig. 1). A fiberglass window screen (permeability of 70%) was installed in this area and black-tape patches of the same type and size as in Area 1 were mounted at uniform intervals on the screen. The temperature targets in Areas 1 and 2 were installed during a scheduled shutdown of the valve hall. More details can be found in [17].

2.5.3. Experimental setup and procedure

After regular operation resumed in the valve hall, the equipment was allowed to come into thermal equilibrium with the room during a two-week period before testing was conducted. The first step was to record the operating conditions in the valve hall related to the experiment (this step was performed at the beginning and the end of the experiment and the data were found to be the same). The recorded operating conditions included the mass flow rate, the inlet, and the outlet bulk temperatures of the air. Values of V_{jet} and q'' were determined from these data.

The second step was to record the air temperatures in the valve hall 2.5-m away from the towers and within 5-m elevation from the floor. These temperatures were recorded using a Kestrel® 3000 digital thermometer with an accuracy of ±1 °C. These temperatures were recorded at a heights of $z = 1$ m and $z = 4$ m, and regular intervals of x and y. It was found that all temperatures were within ±0.5 °C of a certain value at each height.

The third step of the experiment was to take infrared images in Areas 1 and 2. The infrared camera used for the experiment was a Flir Systems Thermacam® PM 695 with an accuracy of ±2 °C. All electrical lights were turned off during the experiment in order to eliminate them as a possible radiation source. Because the two areas were large in size, each area was photographed in parts in order to increase the resolution of each image. When the experiment was completed, the data were processed using Thermacam Researcher™ 2.8 software and the temperatures at the centre of each black square tape, along with the corresponding location, were recorded.

2.5.4. Experimental results and comparisons

Numerical results were obtained using CD1 with input data for V_{jet}, q'', T_o, and geometry parameters identical to those recorded during the experiment. The angle of inlet air jet, θ, in the existing valve hall was determined to be 60° and this value was used in the model. The medium mesh defined in Section 2.4 was used in the simulation.

Fig. 6 shows a comparison between the experimental and the numerically predicted temperatures on a line in Area 1. The numerical results were computed at both 0.03 m and 0.06 m away from the surface of the tower (i.e., in the y direction) in order to match the conditions of the experiment. Two sets of experimental results corresponding to similar locations on two towers are presented in Fig. 6 and the two sets are practically identical, which confirms the symmetry imposed in the numerical model. The numerical results correctly predict that

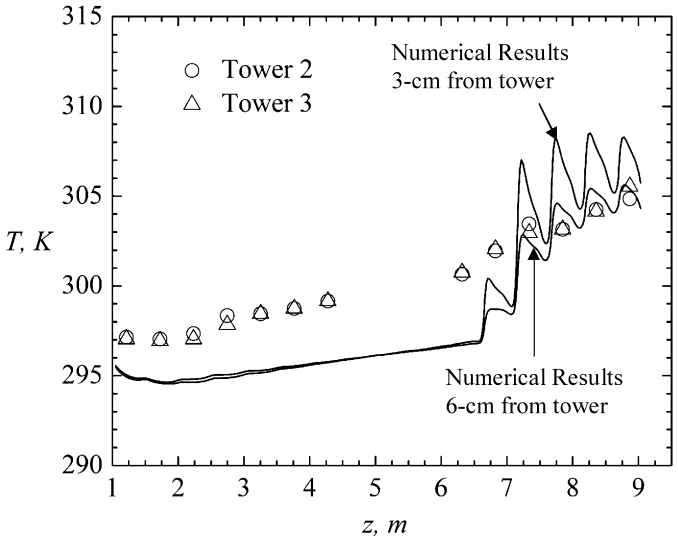

Fig. 6. Comparison of experimental and numerical results in Area 1.

the temperatures near the block faces become higher with increasing height; however, these results somewhat under-predict the temperatures near the bottom of the tower. One possible explanation is that the actual temperature of the air issuing from the inlet opening into the room was higher than the inlet temperature used in the simulation. The inlet air temperature sensor in the valve hall is located in the duct work upstream of the inlet opening and there is a possibility of some heat gain by the air before entering the valve hall. In general, the maximum deviation between the experimental and numerical results is about 3 °C.

Fig. 7 shows temperatures on three lines in Area 2 compared with numerical results. These lines corresponds to $x = 0.37$ m, $x = 1.13$ m, and $x = 1.89$ m. The numerical results along all three lines show good agreement with the experimental results, with the air temperature varying very little with x and y at this height.

3. Results and discussion

Results from seven simulations (Cases A to G) are presented here, and interested readers can find a lot more results in [17]. Case A corresponds to the current operating conditions in the existing valve hall, while cases B to G represent attempts to improve the air distribution, and consequently decrease the temperature level in the valve hall by changing one or more of the geometry and/or inlet conditions. The dimensions defined by numerical values in Figs. 2 to 5 were held constant and, in addition, some other parameters were also held constant as given in Table 1.

Of the seven cases presented here, five were simulated using CD1 (Cases A to E) and two were simulated using CD2 (Cases F and G). Of the five cases with CD1, Cases A to D used an inlet opening located on the floor of the cavity and Case E used an inlet opening located on the side wall. All CD1-simulations used an inlet flow rate $\dot{m}_o = 0.684$ kg/s, consistent with the existing valve hall operating condition, while CD2-

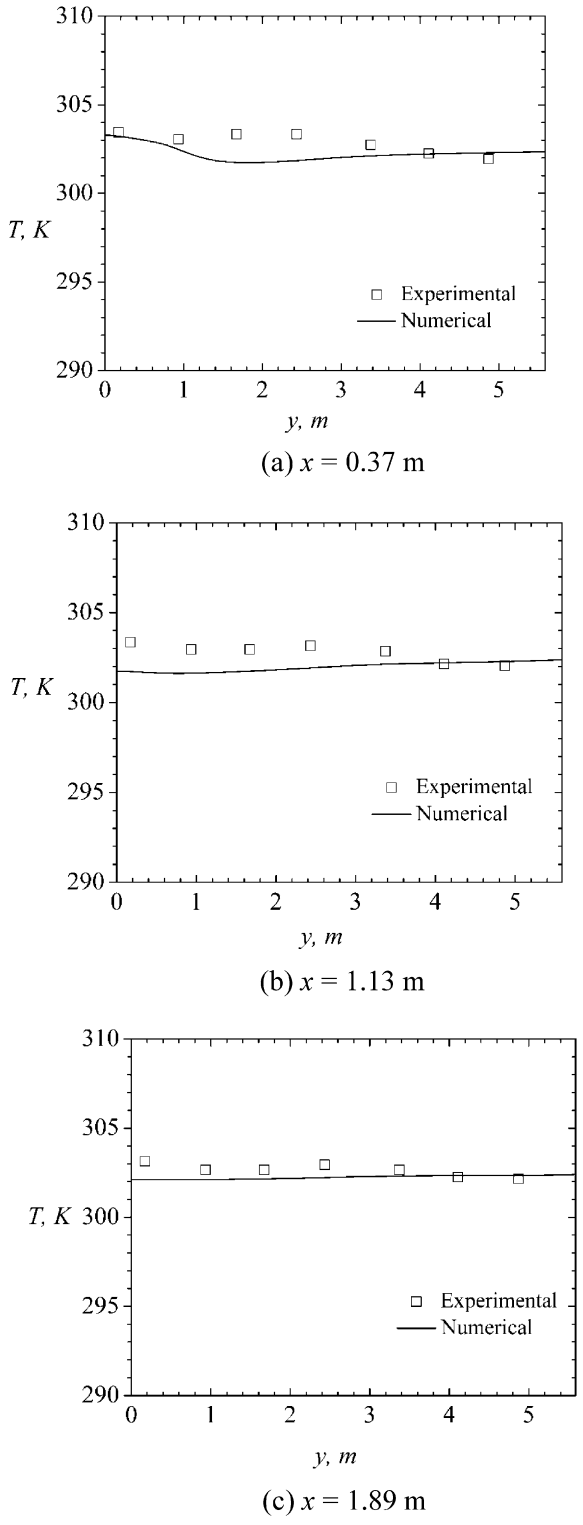

Fig. 7. Comparison of experimental and numerical results in Area 2.

simulations used $\dot{m}_o = 1.368$ kg/s since CD2 has double the volume and double the heat input of CD1.

Among the cases of floor injection, Case A (the base case) corresponds to an inlet angle of the air jet of $\theta = 60°$. Case B explores the effect of changing θ from 60° to 80°, while keeping all other parameters unchanged. Case C explores the effect of increasing the inlet air velocity by just decreasing the area of the inlet grill, while keeping $\theta = 81°$ and all other parameters unchanged. Case D explores the effect of changing the aspect ratio (L_1/L_2) of the inlet grill with $\theta = 80°$ and V_{jet} close to $V_{\text{jet,CA}}$.

The inlet air was injected horizontally in all cases of side-wall injection. In Case E, inlet grills were located on both side-walls at $y = \pm 5.59$ m (see Fig. 1), while Cases F and G correspond to inlet grills on one side wall only. Case G corresponds to nearly half the inlet-grill area of Case F, and therefore, twice the inlet jet velocity. Cases E and G correspond to similar values of L_4, L_5, and L_6, with the main difference being that in Case E there are grills on both side walls while in Case G there are grills on one side wall only with twice the value of V_{jet}.

In addition to symmetry planes S1 and S3, two additional planes (P1 and P2) will be used in presenting the results from simulations with CD1. The location of these planes is shown in Fig. 8. For CD2, three additional planes (Q1 to Q3), shown in Fig. 9, will be used in presenting the corresponding results.

3.1. Base case (Case A) results

Previous research on this topic [6] has clearly established that the temperature level of the heat-generating blocks is directly related to the magnitude of air flow in the gaps between the block and therefore, special attention was paid to this parameter in this study. Because of symmetry on planes S1 and S3, the net mass flow rate of air entering a particular gap on plane P1 must also be equal to the net mass flow rate exiting the same gap on plane P2. Table 2 shows the net mass flow rates for each gap, $|\dot{m}_g|$ in Case A. It should be noted that this method for determining the mass flow rate does not show the direction of the flow and could also possibly be misleading in the case of a significant mass flow rate entering a gap on a plane and exiting the gap on the same plane. The phenomenon of mass entering a gap on one plane and exiting on the same plane generally occurred only when the mass flow rate entering a gap on P1 was low and thus the maximum temperature in that gap was relatively high. Table 2 also shows the net mass flow rate through each gap as a percentage of the total inlet mass flow rate, as well as the maximum temperature in each gap, $T_{\max,g}$.

Table 2 demonstrates the poor air distribution through the tower gaps. A total of 72.6% of the inlet mass flow rate passes through Gaps 1 to 5. The maximum temperature in any of these

Table 1
Parameters held constant for all simulations

T_o (°C)	ρ_o (kg m^{-3})	C_p (J kg^{-1} K^{-1})	λ (W m^{-1} K^{-1})	μ (kg m^{-1} s^{-1})	q'' (W m^{-2})	I_o	R_o
21.2	1.2	1004.4	0.0261	1.831×10^{-5}	60.6	0.05	10

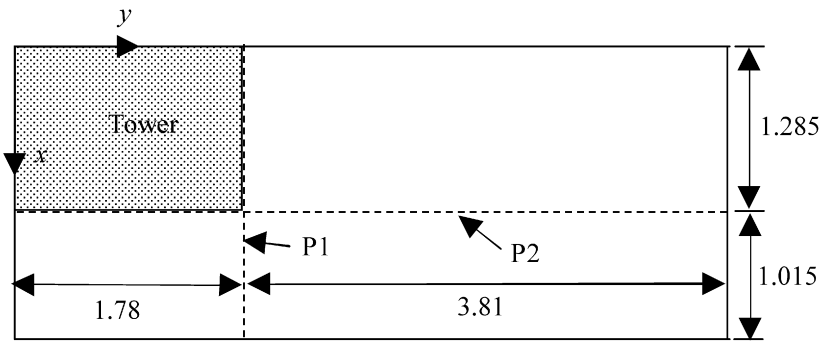

Fig. 8. Location of planes P1 and P2 for CD1 (dimensions in meters).

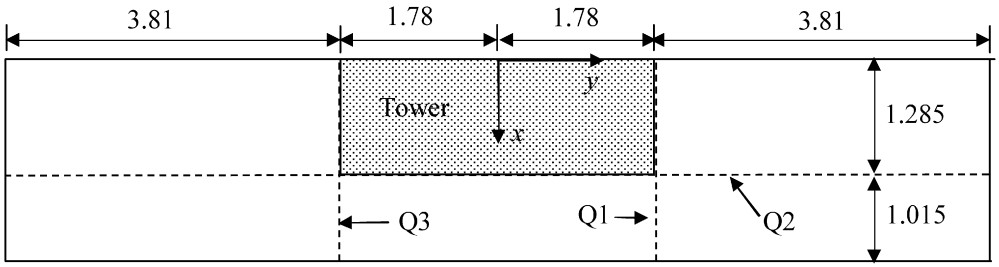

Fig. 9. Location of planes Q1, Q2, and Q3 for CD2 (dimensions in meters).

Table 2
Mass flow rates and maximum temperatures in each gap for Case A

Gap number	$\lvert\dot{m}_g\rvert$ (kg s^{-1})	$\frac{\lvert\dot{m}_g\rvert}{\dot{m}_o} \times 100$	$T_{\max,g}$ (°C)
1	0.1765	25.81	27.57
2	0.1138	16.64	31.68
3	0.0812	11.87	33.38
4	0.0671	9.81	33.20
5	0.0577	8.44	33.78
6	0.0481	7.03	37.55
7	0.0401	5.86	40.44
8	0.0334	4.88	44.58
9	0.0265	3.87	49.53
10	0.0123	1.80	65.78
11	0.0004	0.06	89.44
12	0.0049	0.71	84.40
13	0.0040	0.59	81.52
14	0.0016	0.24	86.33
15	0.0000	0.00	95.37
Total	0.6676	97.61	

gaps is 33.78 °C, occurring in Gap 5. An amount equal to 25.8% of the inlet mass flow rate flows through Gap 1, while only 8.4% of the inlet mass flow rate flows through Gap 5. Even though the mass flow rate through Gap 1 was more than three times that of through Gap 5, the maximum gap temperature only varied by 6.21 °C for these two gaps. Clearly, much more flow than needed passed through Gap 1. A total of 23.4% of the inlet mass flow rate passes through Gaps 6 to 10. The maximum temperature in these gaps is 65.78 °C, occurring in Gap 10. In Gaps 11 to 15, the combined total flow is only 1.6% of the inlet mass flow rate. As a result, the maximum temperature in each of these gaps was greater than 81.5 °C. These results indicate that the maximum temperature in a gap depends highly on the net mass flow rate in that gap.

Only 3.9% of the inlet mass flow rate passes through Gap 9, and yet the maximum temperature is less than 50 °C. If a scheme could be devised in which this mass flow rate passed through each of the fifteen gaps, the tower could be effectively cooled with as little as 58% of the total inlet mass flow rate used in Case A. It is evident from these observations that the higher than desired maximum temperatures in some of the gaps are not a result of the total inlet mass flow rate being too low, but are a result of deficiencies in the local mass flow rates through the gaps containing the high maximum temperatures.

3.2. Enhancement of the cooling effectiveness

Attempts were made to improve the air-cooling effectiveness in the valve hall over the existing conditions (Case A) and the results from six of these attempts (Cases B to G) are presented here. A key feature in Cases B to G is that the inlet air mass flow rate was kept the same as Case A. The geometry and inlet flow conditions, as well as the resulting maximum temperature in the domain and the location of this maximum temperature are presented in Tables 3 to 5.

Cases B to D correspond to floor air injection. In Case B, the only modification (relative to Case A) is a change in the air injection angle from 60° to 80°. Case C involves changing the air injection angle to 81° and decreasing the vents' inlet area to approximately one half the existing value in order to increase the inlet air velocity. Case D explores the effect of changing the aspect ratio of the inlet vents (by decreasing L_1 and increasing L_2) together with changing the air injection angle to 80° and a 22% reduction in the area of inlet vents.

The computed net flow rate and maximum temperature in each of the 15 gaps in the tower for Cases A to D are shown in Fig. 10. Case B produced a reduction in air flow in Gaps 1

Table 3
Summary of Cases A to D (floor air injection with CD1)

Case	L_1 (m)	L_2 (m)	L_3 (m)	θ (deg)	$(\frac{A_o}{A_{o,\mathrm{CA}}})^*$	$(\frac{V_{\mathrm{jet}}}{V_{\mathrm{jet,CA}}})^*$	$T_{\mathrm{max},g}$ (°C)	Gap
A	0.545	0.48	2.67	60	1	1	95.37	15
B	0.545	0.48	2.67	80	1	0.879	86.21	12
C	0.545	0.235	2.67	81	0.49	1.791	78.10	3
D	0.2	1.02	2.42	80	0.78	1.128	80.09	15

* $A_{o,\mathrm{CA}} = 0.2616\ \mathrm{m}^2$; $V_{\mathrm{jet,CA}} = 2.516\ \mathrm{m\,s}^{-1}$.

Table 4
Summary of Case E (side-wall air injection with CD1)

Case	L_4 (m)	L_5 (m)	L_6 (m)	$(\frac{A_o}{A_{o,\mathrm{CA}}})^*$	$(\frac{V_{\mathrm{jet}}}{V_{\mathrm{jet,CA}}})^*$	$T_{\mathrm{max},g}$ (°C)	Gap
E	0.069	8.3	1.38	2.19	0.397	85.54	13

* $A_{o,\mathrm{CA}} = 0.2616\ \mathrm{m}^2$; $V_{\mathrm{jet,CA}} = 2.516\ \mathrm{m\,s}^{-1}$.

Table 5
Summary of Cases F and G (side-wall air injection with CD2)

Case	L_4 (m)	L_5 (m)	L_6 (m)	$(\frac{A_o}{2A_{o,\mathrm{CA}}})^*$	$(\frac{V_{\mathrm{jet}}}{V_{\mathrm{jet,CA}}})^*$	$T_{\mathrm{max},g}$ (°C)	Gap
F	0.156	7.32	1.38	2.183	0.397	62.75	12
G	0.073	7.82	1.38	1.091	0.795	50.11	15

* $A_{o,\mathrm{CA}} = 0.2616\ \mathrm{m}^2$; $V_{\mathrm{jet,CA}} = 2.516\ \mathrm{m\,s}^{-1}$.

to 5 and a corresponding increase in the maximum temperature (relative to Case A). The reverse happened in Gaps 6 to 11 and a mixed trend can be seen in Gaps 12 to 15. Overall, the maximum temperature in the domain for Case B is 86.21 °C, about 9 °C reduction from Case A by a simple change in the air jet angle. Case C corresponds to about double the value of V_{jet} as in Case B while maintaining a similar value of θ. Fig. 10 shows further reduction in air flow in Gaps 1 to 5, but a substantial increase in air flow in Gaps 6 to 15. This has translated into lower temperatures in the upper gaps, with $T_{\mathrm{max},g}$ less than 45 °C in Gaps 6 to 15, but higher temperatures in the lower gaps with $T_{\mathrm{max},g} = 78.10$ °C in Gap 3. Finally, Case D shows the effect of changing the aspect ratio of the inlet vents. Fig. 10 shows that $\dot{m}_g/\dot{m}_o$ is 2.5% or higher in Gaps 1 to 12 and, as a result, $T_{\mathrm{max},g}$ is lower than 50 °C in all these gaps. In Case D, the highest value of $T_{\mathrm{max},g}$ is 80.09 °C, and it occurs in Gap 15 where the air flow rate is minimum.

The results in Fig. 10 demonstrate that the pattern of air distribution through the gaps of the tower and the resulting temperatures in the tower are very sensitive to the independent parameters θ, A_o, and (L_2/L_1). Substantial reductions in $T_{\mathrm{max},g}$ can be achieved by carefully selecting appropriate values for these independent parameters and this can only be achieved by a detailed CFD analysis similar to the present one.

Cases E to G correspond to side-wall air injection with an inlet jet directed in the horizontal direction. In Case E, the cooling air is injected through vents located on the two walls at $y = \pm 5.59$ m (see Fig. 1), while in Cases F and G, the cooling air is injected through vents located only on the wall at $y = 5.59$ m. The inlet area of the vent for Case E is about twice

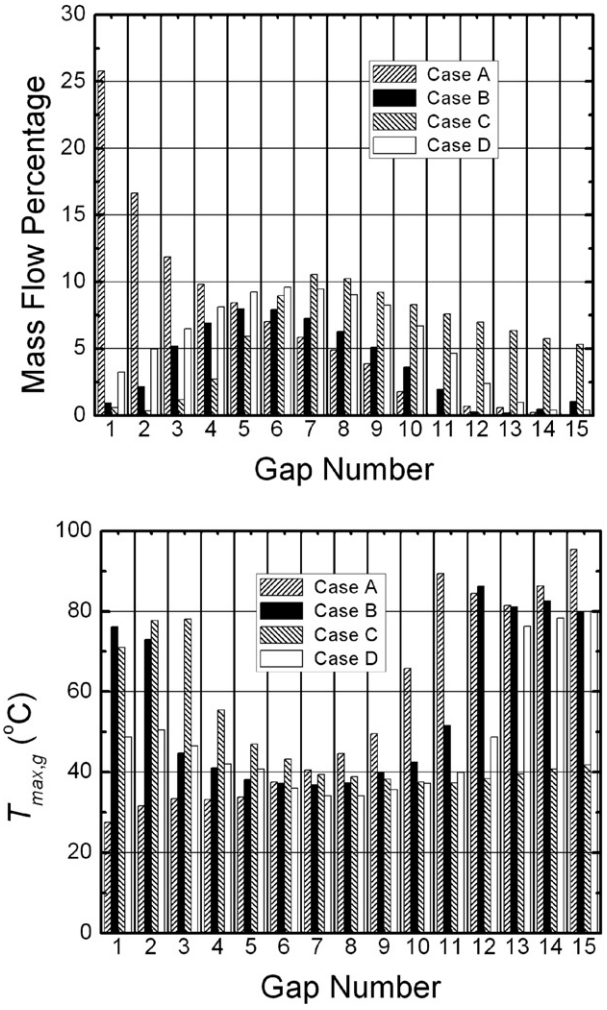

Fig. 10. Air flow rates and maximum temperatures in all tower gaps for Cases A to D.

the vent area of Case A. Two different vent areas are simulated in Cases F and G.

For Case E, air flow issuing from the inlet opening has a tendency to descend as it progresses towards the tower due to the density difference between the surrounding air and the cooling air. As a result, the highest overall mass flow rate and lowest maximum gap temperature occur in Gap 1. The overall mass flow rate though each gap decreases with increasing gap number for Gaps 1 to 9. The net mass flow rate through these gaps was high enough, however, that the maximum temperature in Gaps 1 to 9 was 55.65 °C (occurring in Gap 7). In Gaps 10 to 15, there is a higher mass flow rate entering the gap through

plane P2 and exiting the gap through P1. This is the reverse flow pattern of Gaps 1 to 9. There are a number of factors that contribute to the reversal of flow in Gaps 10 to 15. Air exiting Gaps 1 to 9 through P2 rises because its temperature is higher than that of the surrounding air, causing a large amount of air to pass next to the opening to the upper gaps on P2. Because the inlet air has a tendency to descend as it progresses towards the towers, there is no rising plume of air near P1 for these gaps. As a result, some of the air passing by the upper gaps on P2 has a tendency to be pulled through the gap, causing this reversed flow pattern. Because the magnitude of the mass flow rate of this air is still relatively low in Gaps 10 to 15, the maximum temperatures in these gaps are relatively high with the maximum domain temperature being 85.54 °C in Gap 13. It is interesting to note that Gap 13 is not the gap where the lowest net mass flow rate occurs. The lowest individual gap net mass flow rate occurs in Gap 10. The maximum temperature in this gap (68.61 °C), however, is noticeably lower than in Gap 13. Examination of the flow through this gap shows that some of the air issuing from the inlet opening enters Gap 10 on P1 and an almost equal amount of flow exits this gap on the same plane, thus resulting in a low net mass flow through the gap. This is an example of a situation where the net mass flow rate through a gap can be misleading. Overall, Case E achieved nearly a 10 °C reduction in maximum domain temperature compared with Case A. However, Cases C and D with floor air injection produced better cooling effectiveness than Case E.

For Cases F and G (using CD2), there are three planes (Q1, Q2, and Q3) through which flow can enter or exit a gap. Since mass must be conserved, the net mass flow rate entering a gap must also be equal to the net mass flow rate exiting the same gap. The flow rates entering or exiting each gap through planes Q1, Q2, and Q3 were calculated and the largest of the three amounts is shown in Fig. 11 (as a percentage of the total inlet flow) in order to indicate the magnitude of ventilation in the gaps.

As in Case E, air issuing from the inlet opening for Case F also had a tendency to descend as it progressed towards the towers due to the density difference between the surrounding air and the cooling air. Consequently, Gaps 13 to 15 received lower amounts of ventilation than the lower gaps. On the other hand, Gaps 1 to 12 received significant amounts of ventilation resulting in low temperatures in all these gaps. The maximum domain temperature for Case F is 62.75 °C occurring in Gap 12. The reason for the hottest temperature occurring in Gap 12 for this case and not in Gaps 13 to 15 is that the flow entering Q1 on Gap 12 does not penetrate very far into the gap before exiting through Q2. In addition, very little flow enters Gap 12 on Q3. This creates a relative hot spot in this gap near Q3.

For Case G, where the inlet horizontal velocity is almost twice as large as the inlet velocity for Cases E and F, the flow does not descend as much near the inlet as it did in Cases E and F. As a result, flow directly issuing from the inlet opening enters Gaps 1 to 14 on Q1, with the net mass flow rate entering the gaps on this plane. Some of the cooling air that enters these gaps on Q1 passes through the entire gap and exits on Q3. As result, the net flow rate through the same gaps on Q3 is out

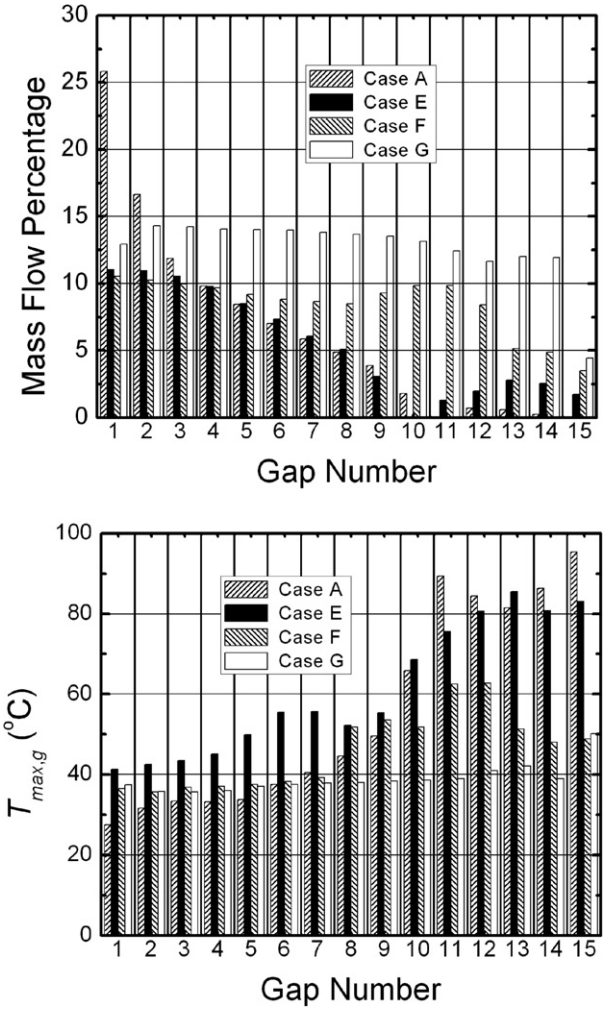

Fig. 11. Air flow rates and maximum temperatures in all tower gaps for Cases A, E, F and G.

of the gaps and no hot spots occur in any of these gaps. The maximum temperature in Gaps 1 to 14 is 42.11 °C, occurring in Gap 13.

The inlet air jet is below the level of Gap 15 by the time it reaches the towers in Case G. As a result, none of the air from the inlet opening passes directly through Gap 15 without first passing through other gaps. For Gap 15, the flow pattern is reversed compared with the first 14 gaps with a net mass flow entering the gap on Q2 and Q3 and exiting the gap on Q1. The maximum temperature in Gap 15 is 50.11 °C. This is also the maximum temperature in the domain. The pattern of flow through the tower gaps and the resulting temperature level in the tower blocks for Case G are far superior to all other cases considered in this investigation.

4. Concluding remarks

A numerical investigation was conducted in order to model the three-dimensional mixed convection during turbulent flow of air in a thyristor valve hall. The effects of the method of cooling-air injection (either from the floor or the side wall), inlet opening geometry (area and aspect ratio), and inlet-air injection

angle on the thermal performance for the air-side cooling of the thyristor valve hall were examined. A base case simulating the currently existing conditions in the valve hall was computed and high temperatures were noted in the upper tiers of the valve tower. In an attempt to identify strategies for alleviating this problem of overheating, six other simulations were performed: three with floor air injection and three with side-wall injection. The comparison between these six cases and the base case was based on the same mass inlet flow rate of air. From these results, the following conclusions can be drawn:

1. The temperature level on the blocks' surfaces in a particular gap depends heavily on the mass flow rate of air in that gap.
2. When the inlet and outlet openings are located as they are in CD1, only moderate improvements in the cooling effectiveness can be made by varying the inlet air angle, and the area and aspect ratio of the inlet vent.
3. When the inlet and outlet opening are located as they are in CD2, dramatic decreases in domain temperature can be achieved compared with the base case.

Acknowledgements

This research has been funded by grants from Manitoba Hydro and the Natural Sciences and Engineering Research Council of Canada. This funding is gratefully appreciated.

References

[1] H.F. Li, B.T. Chung, Mixed convection in a vertical channel with internally heated rectangular blocks, ASME Heat Transfer Division, Fundamentals of Mixed Convection, HTD vol. 274 (1994) 9–16.

[2] S.Z. Shuja, B.S. Yilbas, M.O. Igbal, Mixed convection in a square cavity due to heat generating rectangular body—Effect of cavity exit port locations, International Journal of Numerical Methods for Heat & Fluid Flow 10 (2000) 824–841.

[3] M.T. Bhoite, G.S. Narasimham, M.V. Krishna-Murthy, Mixed convection in a shallow enclosure with a series of heat generating components, International Journal of Thermal Sciences 44 (2005) 121–135.

[4] O. Bellache, M. Ouzzane, N. Galanis, Coupled conduction, convection, radiation heat transfer with simultaneous mass transfer in ice rinks, Numerical Heat Transfer, Part A: Applications 48 (2005) 219–238.

[5] O. Bellache, M. Ouzzane, N. Galanis, Numerical prediction of ventilation patterns and thermal processes in ice rinks, Building and Environment 40 (2005) 417–426.

[6] O.A. Ramirez-Iraheta, H.M. Soliman, S.J. Ormiston, Effective cooling of heat generating stacks in a cavity with openings, Heat and Mass Transfer 42 (2006) 398–410.

[7] J.R. Berg, H.M. Soliman, S.J. Ormiston, Turbulent mixed-convection cooling of stacked heat-generating bodies in a three-dimensional domain, Numerical Heat Transfer, Part A: Applications, in press.

[8] B.E. Launder, D.B. Spalding, The numerical computation of turbulent flows, Computational Methods in Applied Mechanics and Engineering 3 (1974) 269–289.

[9] H. Grotjans, F.R. Menter, Wall functions for general application CFD codes, in: ECCOMAS 98 Proceedings of the Fourth European Computational Fluid Dynamics Conference, Athens, Greece, 1998, pp. 1112–1117.

[10] J.R. Berg, S.J. Ormiston, H.M. Soliman, Prediction of the flow structure in a turbulent rectangular free jet, International Communications in Heat and Mass Transfer 33 (2006) 552–563.

[11] W.R. Quinn, Turbulent free jet flows issuing from sharp-edged rectangular slots: The influence of slot aspect ratio, Experimental Thermal and Fluid Science 5 (1992) 203–215.

[12] S.V. Patankar, Numerical Heat Transfer and Fluid Flow, Hemisphere, New York, 1980.

[13] C.M. Rhie, W.L. Chow, Numerical study of the turbulent flow past an airfoil with trailing edge separation, AIAA Journal 21 (1983) 1525–1532.

[14] C. Prakash, S.V. Patankar, A control volume-based finite-element method for solving the Navier–Stokes equations using equal-order velocity–pressure interpolations, Numerical Heat Transfer 8 (1985) 259–280.

[15] G.E. Schneider, M.J. Raw, Control volume finite-element method for heat transfer and fluid flow using colocated variables: I—Computational procedure; II—Application and validation, Numerical Heat Transfer 11 (1987) 363–400.

[16] T.J. Barth, D.C. Jesperson, The design and application of upwind schemes on unstructured meshes, AIAA Paper 89-0366, 1989.

[17] J.R. Berg, Three-dimensional analysis of airflow and temperature in a thyristor valve hall, M. Sc. thesis, University of Manitoba, Winnipeg, Canada, 2006.